Delft University of Technology

Modeling the effects of position dependence in large-absorber x-ray TES microcalorimeters

Wang, Sifan; Bruijn, Marcel; Gottardi, Luciano; Nagayoshi, Kenichiro; Ridder, Marcel; de Wit, Martin; Gao, Jian Rong; Cui, Wei

Important note
To cite this publication, please use the final published version (if applicable).
Please check the document version above.

Modeling the effects of position dependence in large-absorber x-ray TES microcalorimeters

Sifan Wang ⓘ ; Marcel Bruijn ⓘ ; Luciano Gottardi ⓘ ; Kenichiro Nagayoshi ⓘ ; Marcel Ridder ⓘ ;
Martin de Wit ⓘ ; Jian-Rong Gao ⓘ ; Wei Cui ✉ ⓘ

Check for updates

View Online   Export Citation

Articles You May Be Interested In

Optimal filtering of overlapped pulses in microcalorimeter data

J. Appl. Phys. (November 2020)

Performance of Resistive Microcalorimeters and Bolometers

AIP Conf. Proc. (September 2006)

Array-compatible transition-edge sensor microcalorimeter γ -ray detector with 42 eV energy resolution at 103 keV

Appl. Phys. Lett. (September 2006)

Modeling the effects of position dependence in large-absorber x-ray TES microcalorimeters

View Online   Export Citation   CrossMark

Sifan Wang,[1] Marcel Bruijn,[2] Luciano Gottardi,[2] Kenichiro Nagayoshi,[2] Marcel Ridder,[2]
Martin de Wit,[2] Jian-Rong Gao,[2,3] and Wei Cui[1,a)]

AFFILIATIONS

[1]Low-Temperature Detector Laboratory, Department of Astronomy, Tsinghua University, Beijing 100084, China
[2]Space Research Organization Netherlands (SRON), Niels Bohrweg 4, 2333 CA Leiden, The Netherlands
[3]Optics Group, Department of Imaging Physics, Delft University of Technology, 2628 CJ Delft, The Netherlands

[a)]Author to whom correspondence should be addressed: cui@tsinghua.edu.cn

ABSTRACT

We present finite element simulations of the transition-edge sensor (TES) microcalorimeter behavior using COMSOL Multiphysics. The simulated detector has a large absorber with a size of $990 \times 990 \, \mu m^2$. The simulation calculates the TES response after x-ray impact for a single pixel with a known, realistic, current-dependent resistive transition $R(T, I)$. The simulation includes the full electrothermal feedback effects and heat conduction through the multiple contact points of the absorber to the TES thermometer and supporting membrane. The presented model, especially the 2D model, has been optimized for high accuracy, making it suitable for simulating the detector response when incident photons hit different positions on the absorber. We study the effects of position dependence using Principal Component Analysis with the aim of extracting correct photon energies from the pulses. The simulations show that the degradation, i.e., the FWHM broadening, due to the pulse variations will be less than 0.7 eV at below 2 keV, while it can be significant (>1 eV) at a higher energy band. The simulation result for position dependence can guide the design of large-absorber detectors for future x-ray missions, such as the Hot Universe Baryon Surveyor.

I. INTRODUCTION

The transition-edge sensor (TES)[1] microcalorimeter is a low-temperature detector consisting of three basic components common to all microcalorimeters: (a) an absorber, to stop and thermalize incident photons, (b) a thermometer, to sense the temperature change caused by the photons and convert it to an electrical signal to be read out, and (c) a weak thermal link between the detector and the thermal bath, to drive the detector back to equilibrium to be ready for subsequent photons. Absorbers used with TESs are frequently cantilevered metallic films supported by metallic stems. TES thermometers are typically made of a superconducting bilayer based on the proximity effect. The weak link is commonly formed by fabricating the detector on a suspended silicon nitride membrane. Figure 1 shows a schematic of the TES microcalorimeter used in this study.

With the pulse amplitude being dependent on the photon's energy, the energy resolution of a microcalorimeter is determined by the variation in pulse amplitudes for a specific photon energy. It

is fundamentally constrained by the thermodynamic fluctuation noise, including Johnson noise arising from both TES and other electrical elements, and thermal noise due to fluctuations between thermal elements. The energy resolution achievable with a TES microcalorimeter can be expressed as[1,2]

$$\Delta E_{FWHM} \simeq 2\sqrt{2\ln 2}\sqrt{\frac{4k_B T_0^2 C}{\alpha}\sqrt{\frac{n\xi(I)F(T_0, T_{bath})}{1 - (T_{bath}/T_0)^n}}}, \quad (1)$$

where k_B is the Boltzmann constant, T_0 is the operating temperature of the detector, T_{bath} is the temperature of the heat sink, C is the heat capacity at T_0, α is the temperature sensitivity of the TES, i.e., $\alpha = d\ln R/d\ln T$, n is the thermal conductance exponent related to the heat transfer mechanism of the thermal link between TES and the heat sink, and $F(T_0, T_{bath})$ is a unitless function that depends on n, and $\xi(I)$ is the factor that accounts for the non-linearity in Johnson noise. For a TES, $n \simeq 3 - 4$,
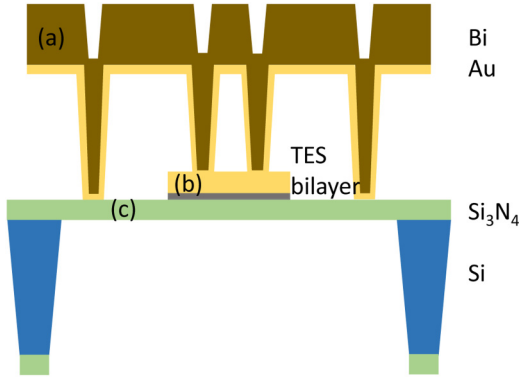
FIG. 1. Schematic of the side view of the TES microcalorimeter: (a) absorber, (b) TES thermometer, and (c) weak thermal link. The size is not to scale.

$F(T_0, T_{bath}) \simeq 0.5 - 1$. In practice, the energy resolution is also affected by other sources of noise, such as electronic readout noise and the position dependence of pulses. For TES microcalorimeters working in the soft x-ray band, example values of these parameters that have been reported are $T_0 \lesssim 90$ mK, $C \simeq 0.8$ pJ/K, and $\sqrt{\xi(I)}/\alpha \simeq 0.02$, leading to the achievement of $\simeq 1.6$ eV energy resolution at 5.9 keV.[3,4] Owing to its exceptional detection performance and scalability to large, multiplexed arrays compared to the microcalorimeter based on a doped silicon thermometer, the TES microcalorimeter has emerged as the primary detector choice for next-generation x-ray astronomy space missions, such as the Advanced Telescope for High ENergy Astrophysics (ATHENA)[5–7] and the Hot Universe Baryon Surveyor (HUBS).[8–10]

HUBS is a proposed space-borne x-ray observatory for the 2030s. The primary scientific objective of the mission is to study the ecosystem of galaxies by directly detecting x-ray emissions from cosmic diffuse hot gas in the energy range of 0.1–2 keV. To achieve its scientific objectives, HUBS will carry a TES microcalorimeter array with 2 eV energy resolution and high absorption efficiency (>90%), and an optical system with 1 arcmin angular resolution (half power angle diameter), 2100 mm focal length and 1 deg^2 field of view (FoV), which will significantly enhance HUBS's capability to observe diffuse x-ray emissions. Due to the limitation of the total number of pixels that can be read out, primarily constrained by wiring density and thermal load considerations, the surface area of the x-ray absorber in TES microcalorimeter pixels must be as large as 1 mm^2 to fully cover the FoV. Bismuth (Bi) is a good choice for the absorber due to its low heat capacity and high x-ray stopping power. However, the thermal conductivity of Bi is poor at low temperatures, so typically, a gold (Au) layer is added to improve the lateral thermalization. To fulfill 2 eV resolution, there is an upper limit to the absorber heat capacity, which translates into an Au layer thickness of less than 130 nm for 1 mm^2 pixel.[10] A key concern for large absorbers is whether such a thin layer of Au can maintain sufficiently good thermal conductivity[11] to minimize the position dependence of pulse shape, which will degrade the detector energy resolution. Previous measurement[11–13] and simulation[14–17] works have shown that the energy resolution

degradation due to position dependence can be significant for absorbers with low thermal conductivity.

To arrive at a reliable optimization for large-absorber detectors, we use COMSOL Multiphysics[18] to perform sophisticated finite element analyses of large-absorber microcalorimeters and investigate the effect of position dependence on the energy resolution using Principal Component Analysis (PCA). The traditional method of microcalorimeter pulse processing is the optimal filtering,[19] which is valid only under the condition of stationary noise and linear response. As a non-parametric approach, the PCA method decomposes and re-expresses the pulse dataset with the eigenvectors of its covariance matrix and reveals its hidden structure. Several groups have investigated its application to the analysis of microcalorimeter pulses,[20–23] dealing with non-stationary noise and non-linear response of microcalorimeter pulses, e.g., non-linear saturation, outliers, and pulse shape variation due to position dependence.

II. MODEL DESCRIPTION

Figure 2 shows the diagram of the thermal and electrical circuits implemented in the simulation. The thermal part of the displayed diagram is a simplification, employing lumped-sum parameters, which has been widely used by the community and can be solved by traditional methods for coupled differential equations. In our case, this lumped sum will be separated in a continuous 3D or 2D spatially varying parameter set. $C(T)$ denotes the detector heat capacity, $G(T)$ the thermal conductance of the weak thermal link, and T_{bath} the temperature of the thermal bath. The TES is connected in series with an inductor L and in parallel with a small shunt resistance R_{shunt}. They are biased via a DC source V_{bias} and a large bias resistance R_{bias}. The corresponding differential equations are[1]

$$C(T)\frac{dT}{dt} = P_{Joule}(T, I) - P_{bath}(T) + P_{photon}, \quad (2)$$

$$L\frac{dI}{dt} = R_{shunt}(I_{bias} - I) - IR_{TES}(T, I), \quad (3)$$

where P_{photon} is the power of the incident photon, $P_{Joule} = I^2 R_{TES}(T, I)$, $P_{bath} = K(T^n - T_{bath}^n)$, and K is a constant factor. The TES resistive transition surface $R_{TES}(T, I)$ used in the simulation, as shown in Fig. 3, is fitting to the data calculated for a
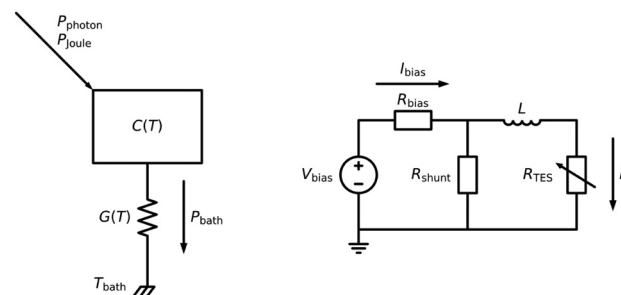

FIG. 2. Diagram of the thermal and electrical circuits implemented in the simulation.
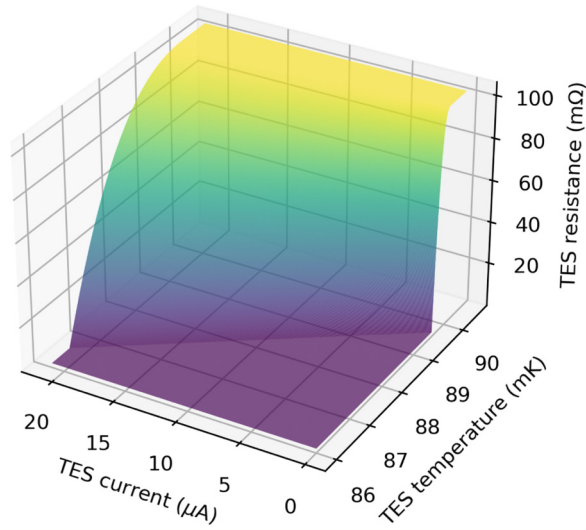
FIG. 3. $R_{\text{TES}}(T, I)$ surface used in the simulation.

Ti/Au TES microcalorimeter developed at SRON, based on the resistively shunted junction (RSJ) model.[24] Both temperature sensitivity and current sensitivity have been considered; therefore, the full effect of electrothermal feedback has been included in the simulation. P_{bath} describes the heat transfer between the detector and the thermal bath. Previous studies have shown that the dominant thermal transfer mechanism in such silicon nitride membrane structure is in the form of ballistic phonon transport at temperatures around 100 mK; thus, in our case, P_{bath} can be expressed as a radiative power,[25]

$$P_{\text{rad}} = \sigma A \zeta \left(T^4 - T_{\text{bath}}^4 \right), \tag{4}$$

where $\sigma = 157\,\text{W/m}^2/\text{K}^4$ is the Stefan–Boltzmann constant for transverse and longitudinal acoustic modes in silicon nitride, A is the phonon emitting area defined as the product of the perimeter of the

TES and the thickness of the silicon nitride membrane, and ζ is the transport efficiency. In the simulation, we assume a pure ballistic transport and $\zeta = 1$. Effects such as electron–phonon coupling and Kapitza interfaces have been estimated, but they are two orders of magnitude lower than the radiative phonon transport on limiting thermal conduction and thus neglected in the simulation. For the supporting stem that sits on the silicon nitride membrane, we applied a similar radiative heat flux from its boundary, where A becomes the product of the perimeter of the stem and the thickness of the silicon nitride membrane. Although the model is based on DC bias operation, the detector behavior is expected to have only a slight difference under AC bias; thus, the model is designed to be adaptable for AC bias applications as well.

The detector normally has a lateral size of hundreds of micrometers, while the vertical size is two orders of magnitude smaller. In such a high aspect ratio structure, we expect that the thermal transfer along the vertical direction is much faster than that along the lateral ones; thus, we can choose a 2D model instead of 3D to speed up the calculation. To verify this assumption, we build both 3D and 2D models in COMSOL. As shown in Fig. 4, the TES is located at the center, two absorber stems connect the TES and the absorber, where the TES-absorber coupling follows the typical SRON design,[26] and four supporting absorber stems contact the silicon nitride membrane. One would expect a large number of supporting stems for large absorber detectors to strengthen the mechanical stability, especially during the drying process of the detector fabrication, when the absorber may collapse due to surface tension. However, the thermal leakage through stems will be larger as the total number of stems increases, which will reduce the signal sensed and, therefore, decrease the signal-to-noise ratio. With the help of critical point drying, we can reduce the number of stems while keeping the structure safe;[10,27] thus, we use four stems in our model. In addition, we remove the silicon nitride membrane in both 3D and 2D models since its lateral dimension is no longer a design parameter under ballistic transport according to Eq. (4), and the thermal bath virtually exists under the radiative condition we applied.

As illustrated in Fig. 1, in a real detector, the absorber is an Au/Bi bilayer, and the stem has an "indent" structure instead of a "pillar," due to the layer thickness being a constant. For simplicity,
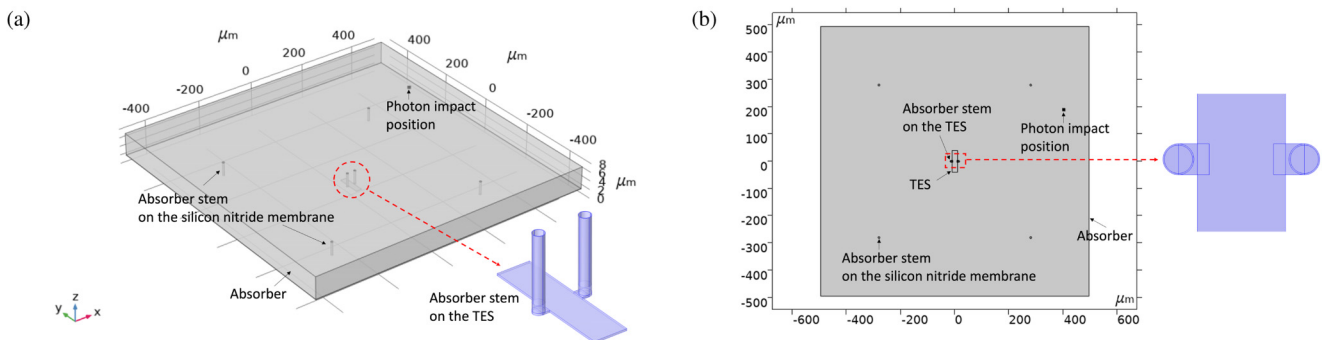

FIG. 4. (a) 3D model with vertical scale extended. (b) 2D model. The zoom-in parts show the connection between the TES and central stems. The stem wall structures are represented by indent cylinders and rings in 3D and 2D models, respectively.
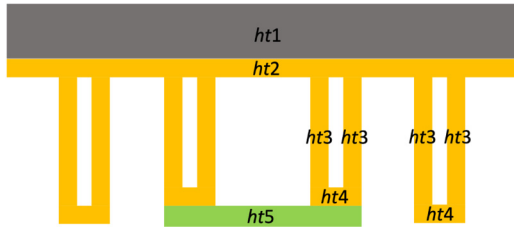
FIG. 5. Schematic of the cross section of the 3D and 2D models. Each layer represents one structure of the detector. In the 2D model, each layer corresponds to one Heat Transfer (*ht*) module in COMSOL. *ht*1: Bi absorber layer; *ht*2: Au absorber layer; *ht*3: Au stem wall layer; *ht*4: Au stem bottom layer; *ht*5: TES layer. In the 3D model, a single *ht* module is used for the entire structure.

in our 3D model, we build the "indents" of the Au layer and planar Au/Bi layer, but disregard the Bi "indents," as illustrated in Fig. 5; we also use vertical stem walls rather than more realistic sloped ones [see the zoom-in part of Fig. 4(a)]. The 3D modeling is quite straightforward in COMSOL. We use single Heat Transfer (*ht*) module for the entire structure (see Fig. 5) to solve Eq. (2). The Joule heating is assigned to the TES, and the radiative power [Eq. (4)] is added to the bottom edge of the TES. An Electrical Circuit (*cir*) module is used to build the electrical circuit as shown in Fig. 2, and Eq. (3) is then solved together by the Electric Currents (*ec*) module which governs the current conservation. To implement 3D structures (i.e., absorber bilayer and "indent" stems) in a 2D model, we first tried a single-layer simplification, by assuming that the Au layer dominates the thermal conductivity. We simplified the Au/Bi bilayer to a single layer and scaled the bilayer heat capacity. We use the same modules as in the 3D model, but this method cannot reproduce 3D simulation results. We finally succeeded by stacking multiple Heat Transfer modules in 2D, representing each physical layer in 3D, instead of using a single module. The schematic of the layer configuration for the 2D model is explained in Fig. 5. Each layer is governed by its own temperature variable instead of a single uniform variable as used in the 3D model. At the connecting area in each 2D layer, we define a heat source and/or a heat sink term, represented by the Kapitza coupling, and the heat rate for layer i can be expressed as

$$P_{\text{Kap},i} = \sum_j K_{ij} A_{ij} \left(T_j^4 - T_i^4 \right), \quad (5)$$

where K_{ij} is the Kapitza coefficient between layer i and layer j, A_{ij} is the contact area of these two layers, T_j is the local temperature of the contact position in layer j, and T_i in layer i. In current simulations, the Kapitza coefficients are set to an arbitrary large value for all layer connections in COMSOL (e.g., $K = 10^{10} \, \text{W/m}^2/\text{K}^4$), which effectively assumes negligible interface resistance. Note that Kapitza coupling is excluded from the 3D model, where it functionally operates as the interlayer connector in the 2D configuration. Such implementation could be a worthwhile refinement in future studies, particularly if the interfacial thermal resistance becomes critical.

TABLE I. Geometric and electrothermal parameters.

Parameter	Value
Thickness of the Si$_3$N$_4$ membrane, $t_{\text{Si}_3\text{N}_4}$	500 nm
Thickness of the Au layer, t_{Au}	100 nm
Thickness of the Bi layer, t_{Bi}	5 μm
Absorber size	990 × 990 μm^2
TES size	80 μm × 20 μm
Height of the stem, h_{stem}	3 μm
Radius of the stem, r_{stem}	3.5 μm
Thickness of the stem wall and bottom	$= t_{\text{Au}}$
Distance of adjacent membrane stems	560 μm
Bath temperature, T_{bath}	53 mK
Bias resistance, R_{bias}	10 kΩ
Bias voltage, V_{bias}	6 V
Shunt resistance, R_{sh}	250 $\mu\Omega$
Circuit inductance, L	0.5 μH
Electrical resistivity of Au at 300 K, $\rho_{\text{Au},300\,\text{K}}$	2.2 $\mu\Omega$ cm
RRR of absorber Au layer, RRR_{Au}[a]	$\dfrac{t_{\text{Au}} \rho_{\text{Au},\,300\,\text{K}}}{(r_s/a_0)^2 \times 9.2 \, \text{nm}}$[11]
RRR of TiAu TES, RRR_{TES}	5
RRR of Au stems, RRR_{stem}[b]	$= RRR_{\text{Au}}$
Electrical resistivity of Bi at 300 K, $\rho_{\text{Bi},300\,\text{K}}$	100 $\mu\Omega$ cm[11]
RRR of absorber Bi layer, RRR_{Bi}	1[11]

[a]Residual-resistivity ratio (RRR) is defined as the ratio of the resistivity of the material at room temperature (300 K) and the working temperature of the detector (e.g., 100 mK). r_s is the radius of the free electron sphere, a_0 is the Bohr radius, t_{Au} is in the unit of nm, and $\rho_{\text{Au},300\,\text{K}}$ is the Au resistivity at room temperature in the unit of $\mu\Omega$ cm.
[b]We treat the absorber stem as the indentation of the absorber Au layer.

The power of the incident photon is modeled as a square function starting at $t = 0.1 \, \mu$s and with a duration $\Delta t = 0.2 \, \mu$s. With a given photon energy E_{ph}, we apply the power $P_{\text{ph}} = E_{\text{ph}}/\Delta t$ to the position of photon impact on the absorber. Key model parameters and their typical values are listed in Table I. Unless otherwise specified, the simulation examples in Sec. III employ the values in the table.

III. RESULTS AND DISCUSSION

A. Internal consistency

The purpose of testing the internal consistency is twofold: to check how precise it could be for studying the position dependence effect and also to check the consistency between the 3D and 2D models. The former is done by calculating the energy content at different photon impact positions across the absorber, including the energy dissipated in the TES (Joule heating), and the extra energy radiated from the boundaries of TES and posts on the membrane, both with respect to the equilibrium; and the latter is done by comparing the simulated pulses with identical model parameters using 3D and 2D models.

Figure 6 shows one example of the different energy contents in the simulation (2D model) varying with time. Due to the law of
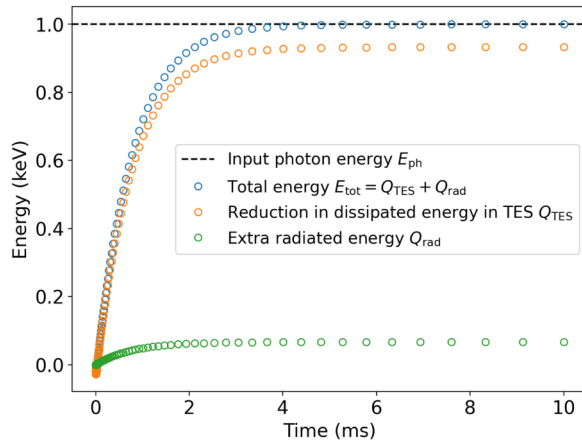
28 July 2025 12:20:16

FIG. 6. Energy contents in the simulation varying with time. The sum of the orange and green circles is equal to the blue one at each time step. The black dashed line indicates the energy of the input photon; the actual impact starts at $t = 0.1\,\mu s$ and lasts $0.2\,\mu s$ in the simulation.

energy conservation, the sum of the reduction in Joule heating in the TES bilayer and excess radiated energy must be equal to the energy of the incident photon after the detector is back in the equilibrium state. We define the model accuracy as the difference between the total energy integrated in the simulation and the energy of the incident photon, i.e., the difference between the blue circle and black dashed line at stationary state in Fig. 6, which is related to the numerical error in the simulation and affected by model solver settings, e.g., solver type, time-stepping, and tolerance, as well as the meshing. With the same solver settings, the accuracy

varies with the photon impact position, i.e., the meshing of every single simulation, and the average accuracy level is ~40 meV @ 1 keV (40 ppm). The distribution of the accuracy at different impact positions across the absorber is shown in Sec. III C.

To illustrate the match between pulse shapes from the 3D and 2D, we choose two different photon impact positions, one near the membrane stem, at coordinate $(250, 280)\,\mu m$, and the other near the TES, at coordinate $(50, 50)\,\mu m$ (refer to Fig. 4). Figure 7 shows the comparison of the pulses. 2D simulations are consistent with 3D simulations, and the maximum deviation in TES current is <0.5%. In Fig. 8, we also compare the calculation time and model accuracy for a single simulation in both 3D and 2D models under different simulation tolerances. Tighter tolerance means higher model accuracy, but it is more time-consuming. For tolerance $>3 \times 10^{-7}$, the 2D model can reach an equivalent or better model accuracy with less calculation time; for tolerance $<3 \times 10^{-7}$, the 3D model is hard to converge while the 2D model can easily reach an accuracy of <10 meV at 1 keV within a short time. In general, the 2D model outperforms the 3D model in calculation time and model accuracy. As a trade-off, we choose a moderate tolerance of 1×10^{-7} in the following position dependency study with 2D models.

B. Comparison with existing measurement

To verify that the model can reproduce the electrothermal behavior of real devices, we compared the simulated pulse with existing experiments at SRON (Fig. 9). The measured detector has an Au/Bi absorber, with a thickness of $2\,\mu m/3.8\,\mu m$ and a side length of $275\,\mu m$, and was characterized using photons from a radioactive ^{55}Fe source. The measured pulse at 5.9 keV has an average rise time of ~7 μs and an average fall time of ~1.1 ms. We used both 3D and 2D models to simulate this detector. The
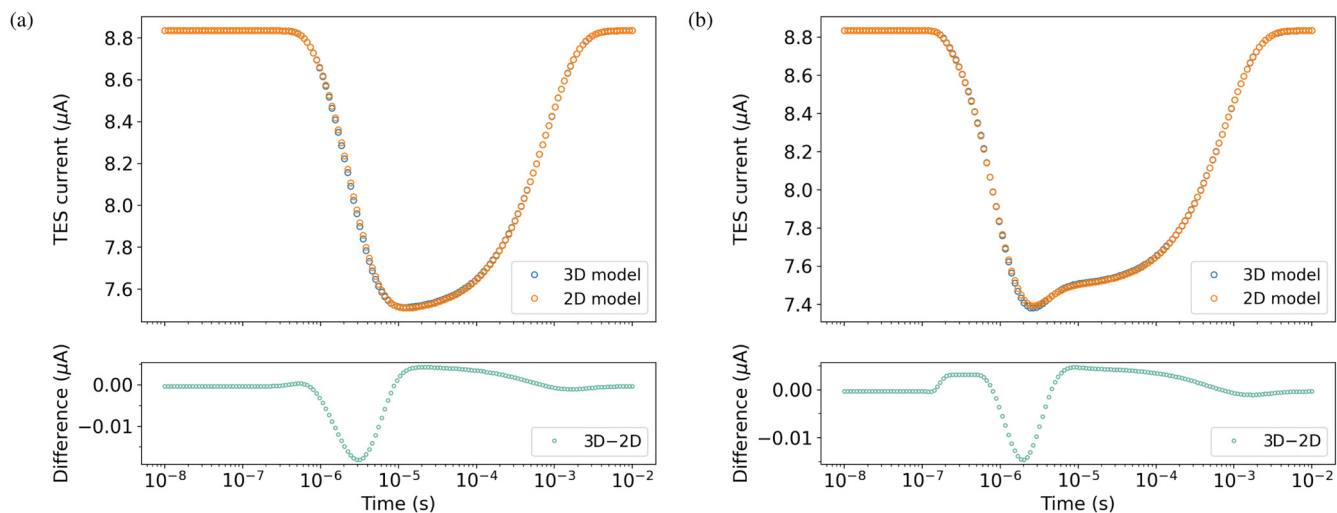

FIG. 7. Comparison of the pulses calculated from 3D and 2D models. The photon impact position in this simulation: (a) near the membrane stem, at $(250, 280)\,\mu m$; (b) near the TES, at $(50, 50)\,\mu m$.
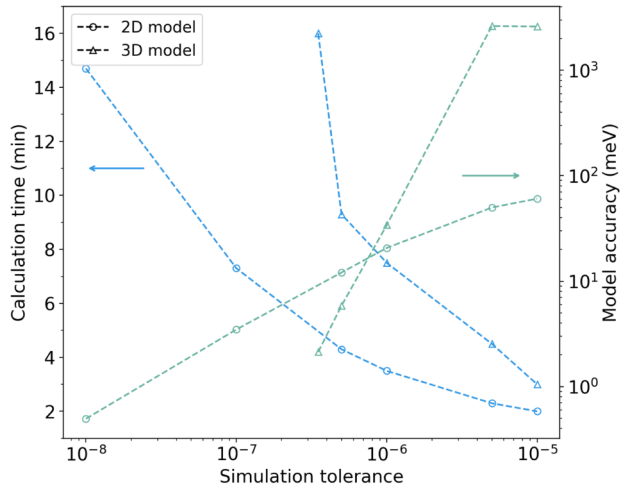
FIG. 8. Comparison between 3D and 2D models regarding calculation time and model accuracy for a single pulse simulation under different tolerance settings.

simulation matches the measurement and has good consistency between 3D and 2D models. Note that in this case $L = 1\,\mu H$, and the position of the central two stems is also on the side of TES, but within the rectangular area, not outside as shown in Fig. 4.

C. Position dependency

To simulate the effect of position dependence on the pulse shape, first, around 4000 photon energies are sampled from the
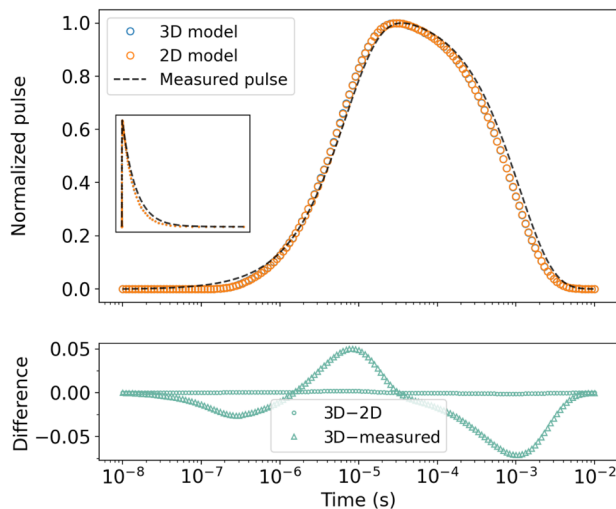

FIG. 9. Measured and simulated pulses. The pulses have been flipped along the x-axis and the heights normalized. The time is represented on a logarithmic scale in the main plot and a linear scale in the inset. The fitting to the averaged measured pulse data is denoted by the black dashed curve.

probability density function for Mn $K\alpha$ and $K\beta$ lines with its natural broadening, the energy is then scaled to the soft x-ray band which we are interested in (e.g., 1 keV, as shown in Fig. 10, the scaled "$K\alpha$" and "$K\beta$" lines). The purpose of selecting this input energy spectrum is to replicate the actual data analysis process as closely as possible, while also facilitating direct comparison with future measurement results (e.g., at 5.9 keV). This method provides multiple peaks for energy calibration for the PCA projection in a single simulation. It also provides a standardized reference point for cross-comparing spectral analyses across different energy ranges (e.g., 0.5–4.5 keV) in separate simulations; second, we randomly put photons with these energies on different positions of the one-quarter area of the absorber [Fig. 11(a)] and calculate the corresponding TES response current pulse [Fig. 11(c)]. We observed a clear delay in the rise of current pulses as the impact position moved away from the center, and pulse spikes for those hit close to the absorber center (roughly within $\sim 150\,\mu m$ radius). This delay is attributed to the limited speed of heat diffusion within the absorber. The absorber consists of an Au/Bi bilayer, but heat diffusion is dominated by that in the Au layer with $RRR_{Au} \simeq 3$. The diffusivity in the absorber in the simulation is calculated as $D = k/C_v$, where k is the thermal conductivity and related to the electrical resistivity according to the Wiedemann–Franz law and C_v is the heat capacity at constant volume. For Au under 100 mK, $D = 0.28\,[W/m/K]/7.2\,[J/m^3/K] \simeq 0.04\,m^2/s$, and the timescale for diffusion toward the center can be estimated as $\tau_{delay} \simeq (L_{abs}/2)^2/D \simeq (990\,[\mu m]/2)^2/0.04\,[m^2/s] = 6\,\mu s$. The rise time is dominated by the bias circuit electrical time constant and is characterized by $\tau_{el} \simeq L/R$. In this case, the average TES resistance during the rise time is 30 mΩ (derived from the resistance variation with time in this simulation), estimation of the rise time will be $\tau_{rise} \simeq \tau_{el} \simeq 0.5\,[\mu H]/30\,[m\Omega] = 17\,\mu s$. The simulation fits both estimations [see Fig. 11(c)]. For a hit very close to the TES, we see an extra dip in the current pulse, this is due to the interaction of the electrothermal feedback with the limited inductance (e.g.,
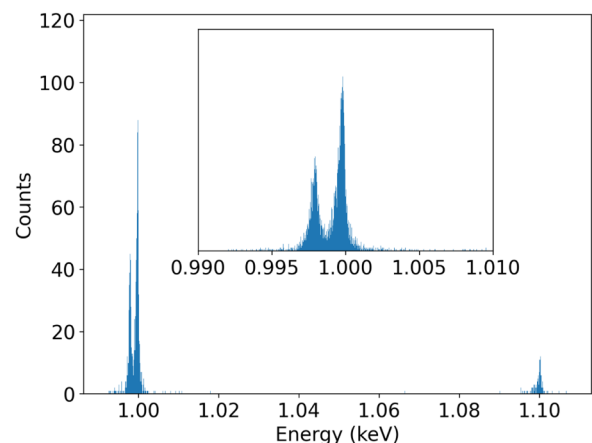

FIG. 10. Input spectrum of the photon energies that sampled from Mn $K\alpha$ and $K\beta$ spectrum and scaled to 1 keV. The inset shows the scaled "$K\alpha$ lines."
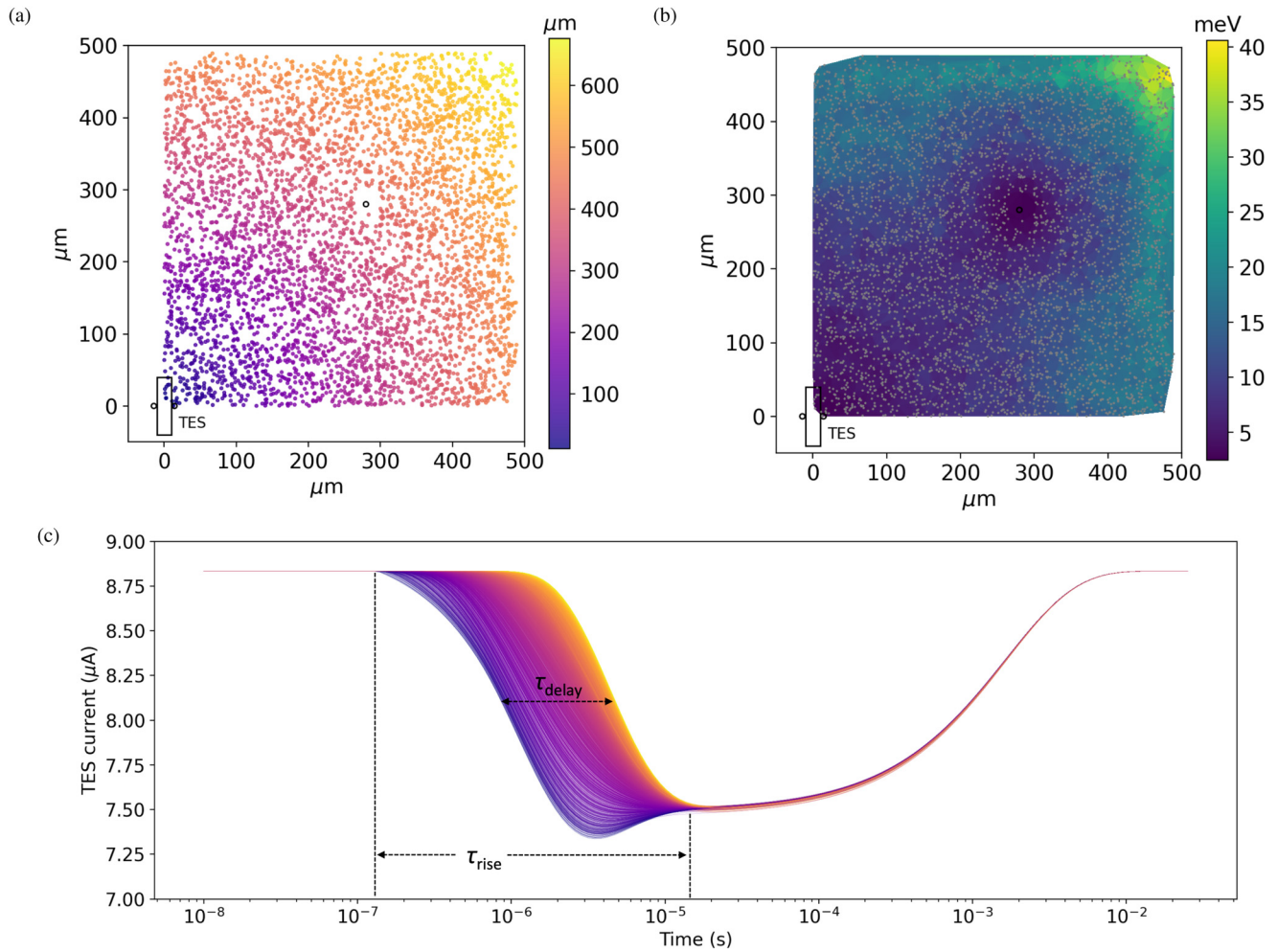
FIG. 11. (a) Around 4000 photons with scaled "Kα" and "Kβ" energies hit randomly on different positions of the one-quarter area of the absorber; (b) model accuracy distribution in this area; (c) simulated TES response currents. The pulses in (c) are attributed to the "Kα" peak in the input energy spectrum [see Fig. 12(a)], and the colors denote the distance to the center of the corresponding impact point.

$\lesssim 0.6\,\mu$H). Heat arrives at the TES almost instantaneously in this region (within $0.1\,\mu$s), causing a rapid temperature change and driving the TES deep into the transition, or even temporarily to the normal state. The inductance, however, does not allow the current to decrease immediately as the resistance increases, so the temperature is boosted by an initial increase in Joule heating, which results eventually in a larger reduction in current in response to the extra power deposited, leading to an overshoot in the TES current. We also check the model accuracy across the area [Fig. 11(b), in this case $\lesssim 40$ meV]. Third, we use PCA to analyze the simulated pulses.[22] Each pulse is projected onto the eigenvectors of the pulse-pulse covariance matrix, and the principal components consist of the first two projections with the largest eigenvalues. Once the correlation of these two principal components is determined, the key information, specifically the pulse energy in this instance, is directly

extracted from the spectrum of the raw pulse dataset projected onto the correlation. Subsequently, we can fit the spectrum to determine its spectral broadening due to position dependence. Detailed results of the PCA applied to the simulated pulses are provided in the Appendix. Figure 12(b) shows an example of the fitting to the "Kα" spectrum of the simulated pulses with $\sim$1 eV excess broadening at 1 keV due to the position dependence effect; the spectrum of the incident photon, which is supposed to have only natural broadening, is also shown in Fig. 12(a) as a comparison. The "Kβ" peak is also fitted and used for the energy calibration in the analysis. Except for a few points at the edges [Fig. 11(b)], the overall model accuracy is smaller than the fitting error of the spectrum. This indicates that our model is well-suited for investigating the spectral broadening due to the position effect.
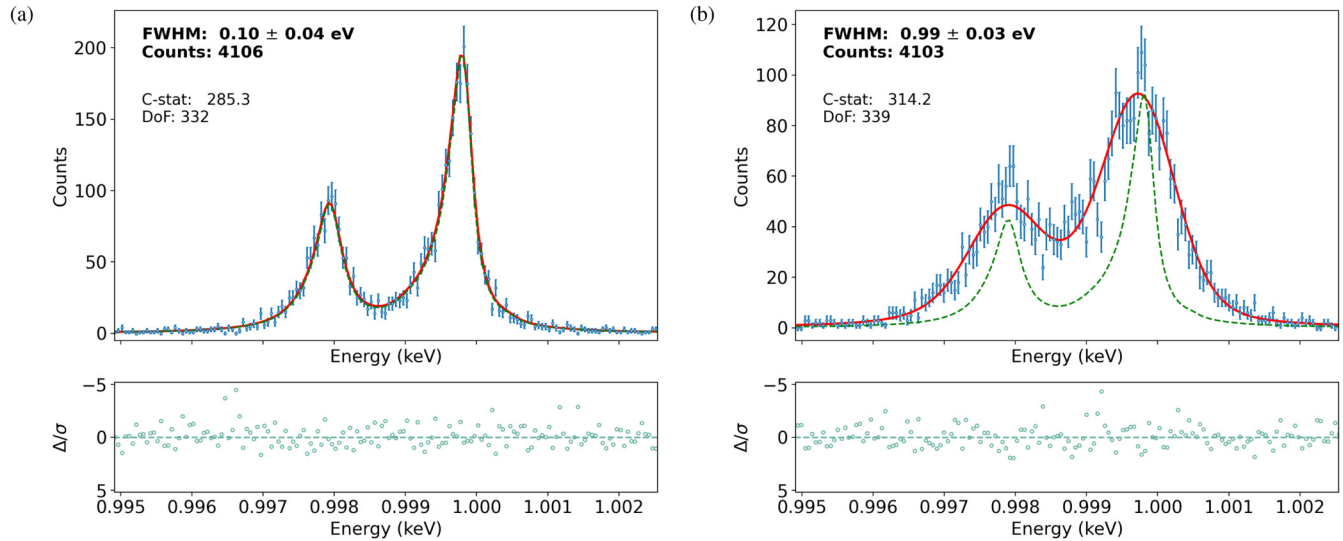
FIG. 12. (a) Spectrum of the incident photon. (b) Spectrum of the output pulses. The green dashed curve indicates the natural broadening of the scaled "Kα" spectrum. The red curve is the fitting to the input/output spectrum. The excess spectral broadening is due to the position dependence effect.

With this model, we performed parameter sweeps for different Au/Bi thickness combinations, circuit inductance (L), and photon energies of interest (E_{ph}), to find an optimized design of the large absorber, which minimizes energy resolution degradation due to the position dependence effect. The relevant results are summarized in Table II.

We first explored the relation between inductance L and excess broadening. With larger L, the rise delay becomes larger, and the pulse shape variation becomes smaller between photon impacts near the center and those further away. As shown in Fig. 13, for our basic design, 1 mm^2 pixel with 100 nm Au/5 μm Bi,

the excess broadening decreases with an increasing L. When the thickness of the Au absorber layer is increased while keeping the same total heat capacity, the excess broadening is only slightly reduced, because of the increased electrical conductivity, thus the thermal conductivity within the absorber. This will decrease the stopping power to a useless low level, because of the simultaneous decrease in the Bi layer thickness. Furthermore, when the Au thickness is increased to 1 μm, the excess broadening becomes even smaller, even with a reduced L down to 50 nH. To achieve the high energy resolution required for HUBS, the heat capacity of the absorber must remain relatively small. Otherwise, the noise

TABLE II. Simulation of the spectral broadening with different model parameters for 990 × 990 μm^2 absorber.

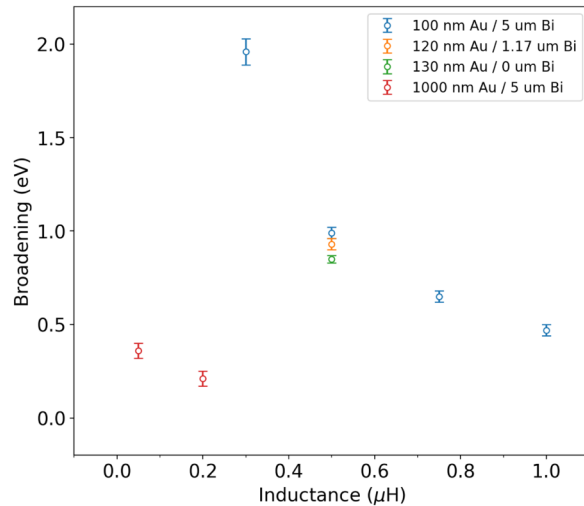| Au/Bi thickness	Heat capacity at 90 mK (pJ/K)	L (nH)	E_{ph} (keV)	Accuracy (meV)	Broadening (eV)
100 nm Au/5 μm Bi	0.80	300	1.0	40	1.96 ± 0.07
		500	1.0	40	0.99 ± 0.03
		750	1.0	40	0.65 ± 0.03
		1000	0.5	10	0.30 ± 0.01
		1000	1.0	40	0.47 ± 0.03
		1000	2.0	70	0.71 ± 0.05
		1000	4.0	160	1.82 ± 0.13
		1000	5.9	270	1.80 ± 0.18
120 nm Au/1.17 μm Bi	0.80	500	1.0	35	0.93 ± 0.03
130 nm Au/0 μm Bi	0.82	500	1.0	40	0.85 ± 0.02
220 nm Au/5.5 μm Bi	1.57	1000	1.5	20	0.38 ± 0.04
		1000	4.5	100	2.02 ± 0.11
		1000	5.9	140	1.95 ± 0.15
1000 nm Au/5 μm Bi	6.49	50	1.0	6	0.36 ± 0.04
		200	1.0	7	0.21 ± 0.04

FIG. 13. Excess broadening due to position dependence with different inductance L at 1 keV "Kα" photon energy.

contribution (which is not modeled here) will become dominant. Consequently, increasing the thickness of the Au absorber layer offers a limited contribution to minimizing the position dependence effect. In contrast, increasing L proves to be a more effective and reliable solution in the simulation. Then, we simulated the excess broadening at different photon energies. As shown in Fig. 14, for our basic design and 1 μH inductance, the overall excess broadening due to position dependence is <0.7 eV under 2 keV

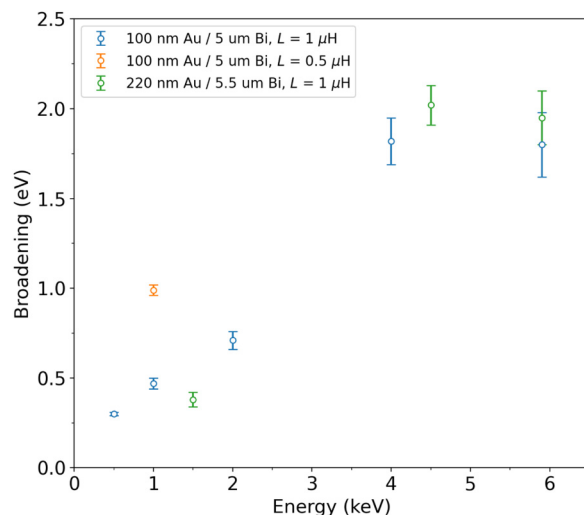**FIG. 14.** Excess broadening due to position dependence at different photon energies.

and becomes $\sim$1.8 eV at higher energies. We also check the 220 nm Au/5.5 μm Bi combination, which will be planned for fabrication in the future, and measured under various x-ray energies, e.g., 1.5, 4.5, and 5.9 keV.

IV. CONCLUSIONS AND OUTLOOK

We present a novel 3D/2D finite-element modeling of TES microcalorimeters using COMSOL, quantifying position-dependent response variations that degrade resolution. Compared to previous finite-element simulation works on such detectors, our study introduces three key advancements: (1) The model includes the full electrothermal feedback effect of TES by implementing the $R(T, I)$ surface, instead of a simple $R(T)$ curve, thereby enhancing physical fidelity. (2) The model has been justified with a high model accuracy, making it sufficient for investigating the position dependence effect in large-absorber detectors, especially with the 2D model. (3) We have provided a method in COMSOL to make the 2D model for such a 3D structure, which saves the calculation time. We use the PCA method to analyze simulated pulses with significant pulse shape variations and extract the energy degradation due to the position dependency effect. For $990 \times 990 \mu$m^2 Au/Bi absorber, with an Au thickness of 100 nm ($RRR_{Au} \simeq 3$) and $L = 1 \mu$H, the degradation due to the pulse variations will be less than 0.7 eV at below 2 keV, while it can be significant (>1 eV) at higher energy band. This simulation provides a tool for designing large-absorber TES microcalorimeters for future x-ray missions like HUBS, offering insights from a purely theoretical perspective. In the next phase, we will analyze the influence of real detector noise on the simulation. This can be accomplished by introducing a broadened input spectrum, for example, for amplifier noise, or by incorporating noise terms into electrical and thermal equations for the noise acting within the electrothermal circuit.[28] Additionally, we plan to investigate the impact of varying stem radii, numbers, and positions on detector performance. Large-absorber detectors are currently in the fabrication process at SRON and Tsinghua University, and we anticipate having measurements soon for comparison with simulation results, as well as for evaluating the differences between optimal filtering and the PCA method when handling pulses from these detectors. The high-throughput capability of large-absorber TES microcalorimeters significantly reduces the required number of pixels, consequently lowering the technical demands on the readout system. The simulation results and subsequent experimental validation will provide valuable insights for broad communities in detector development, scientific instrumentation, and industrial applications.

ACKNOWLEDGMENTS

AUTHOR DECLARATIONS

Conflict of Interest

The authors have no conflicts to disclose.

Author Contributions

Sifan Wang: Formal analysis (lead); Investigation (lead); Writing – original draft (lead); Writing – review & editing (lead). **Marcel Bruijn:** Formal analysis (supporting); Investigation (equal); Supervision (equal); Writing – review & editing (equal). **Luciano Gottardi:** Formal analysis (supporting); Writing – review & editing (equal). **Kenichiro Nagayoshi:** Formal analysis (supporting); Writing – review & editing (equal). **Marcel Ridder:** Resources (supporting). **Martin de Wit:** Writing – review & editing (equal). **Jian-Rong Gao:** Resources (lead); Supervision (lead). **Wei Cui:** Resources (lead); Supervision (lead).

DATA AVAILABILITY

The data that support the findings of this study are available from the corresponding author upon reasonable request.

APPENDIX: PCA OF SIMULATED PULSES

For a set of simulated current pulses, we define a matrix $I_{m \times n}$, consisting of n pulses with m data samples in each pulse. We then construct a new pulse matrix X with a zero baseline: $X_{ij} = I_{ij} - \frac{1}{n}\sum_j I_{ij}$, and calculate its pulse-pulse covariance matrix $C_X = \frac{1}{n}XX^T$. Then, we diagonalize the covariance matrix $C_X = EDE^T$, where E is the matrix of eigenvectors, D is a diagonal matrix with the ith diagonal value being the eigenvalue for the ith eigenvector, sorted from the highest to lowest values. We then project each pulse into the basis of eigenvectors $P = E^T X$, where we get the principal components. By analyzing the correlation in the principal components, we extract energy information and finally calibrate the energy spectrum.

Figure 15 shows the eigenvectors and eigenvalues for the example data (covariance) discussed in the main text. The eigenvectors in Fig. 15(a) reveal the structure of the pulse dataset. The first eigenvector corresponds to the rising part of the pulse; the second eigenvector represents the average pulse shape; the third eigenvector captures variations in the rising part; higher-order eigenvectors describe subtler temporal deviations. Figure 15(b) quantifies the relative magnitudes of the eigenvalues associated with these eigenvectors. It can be seen that the first two eigenvalues dominate, interpreted as encoding the primary information of the dataset, specifically, the photon energy encoded in the pulse. Consequently, they are prioritized for subsequent analysis.

Each pulse is then projected onto the first two eigenvectors (i.e., by computing their inner products), yielding two sets of projection values that define the principal components, as shown in Fig. 16. The horizontal axis represents the indices of all the pulses, while the vertical axis quantifies the projection values onto the eigenvectors. Notably, the projection in Fig. 16(b)
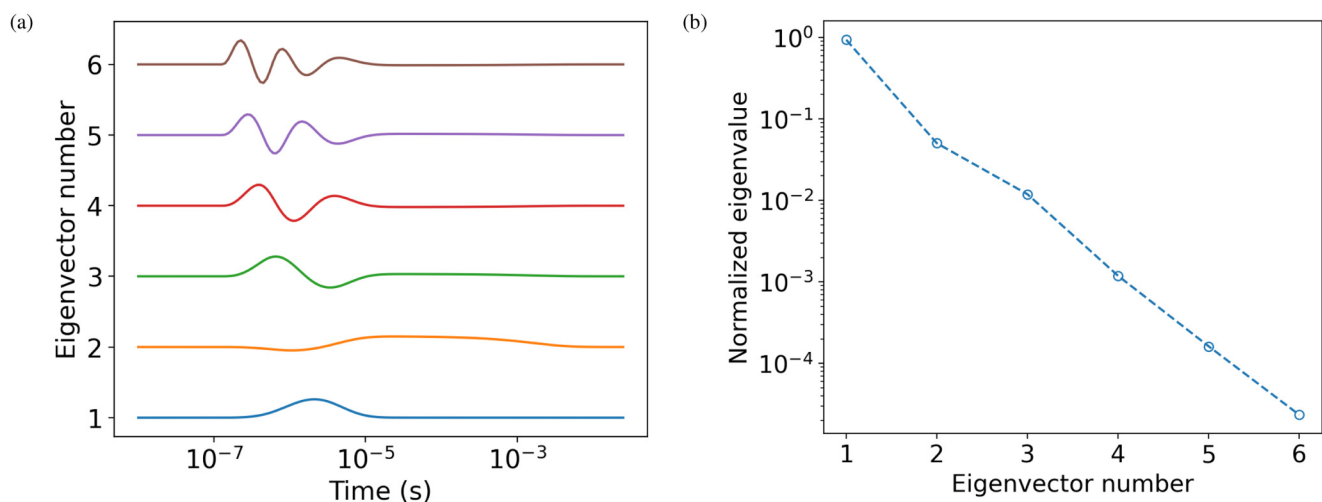

FIG. 15. (a) Eigenvectors and (b) normalized eigenvalues for the example data (covariance) discussed in the main text.
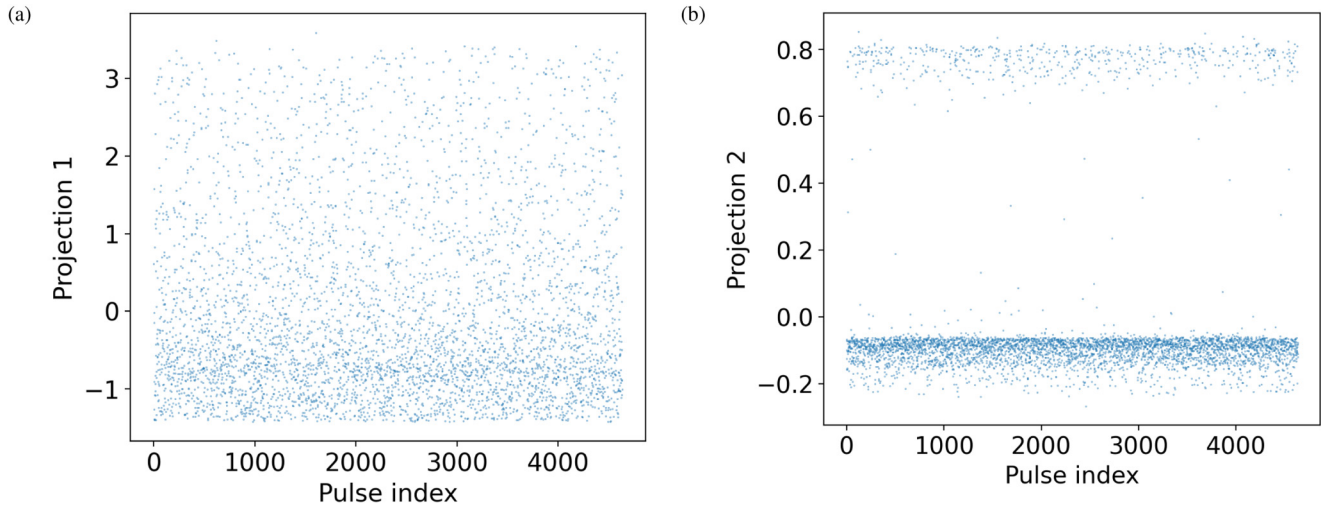
FIG. 16. Projection of all the pulses onto the (a) first and (b) the second eigenvectors.

exhibits a triple-band structure, corresponding to the Kα doublet (two closely spaced lines) and Kβ singlet (single line). This confirms that the second eigenvector, which represents the average pulse shape, encodes the majority of photon energy information.

We then reconstruct the pulses by $X' = EP$, to check the validity of the PCA. Figure 17 shows the results from two different impact positions, thus with different pulse shapes. The reconstruction is good.

The correlation between principal components is quantified in Fig. 18. Here, the color mapping corresponds to the regions defined in Fig. 11(a), indicating the projection of pulses originating from each region onto the eigenvectors. The principal components exhibit strong intrinsic correlations: three parallel clusters emerge, corresponding to the Kα doublet and Kβ singlet. The direction perpendicular to the clusters aligns with the energy calibration axis, while the direction parallel to the clusters reflects consistency with the photon impact positions (indicated by the color). This reveals that the spatial distribution of photon impact dominates pulse shape variations, and these shape variations, in turn, determine the reconstructed energy.
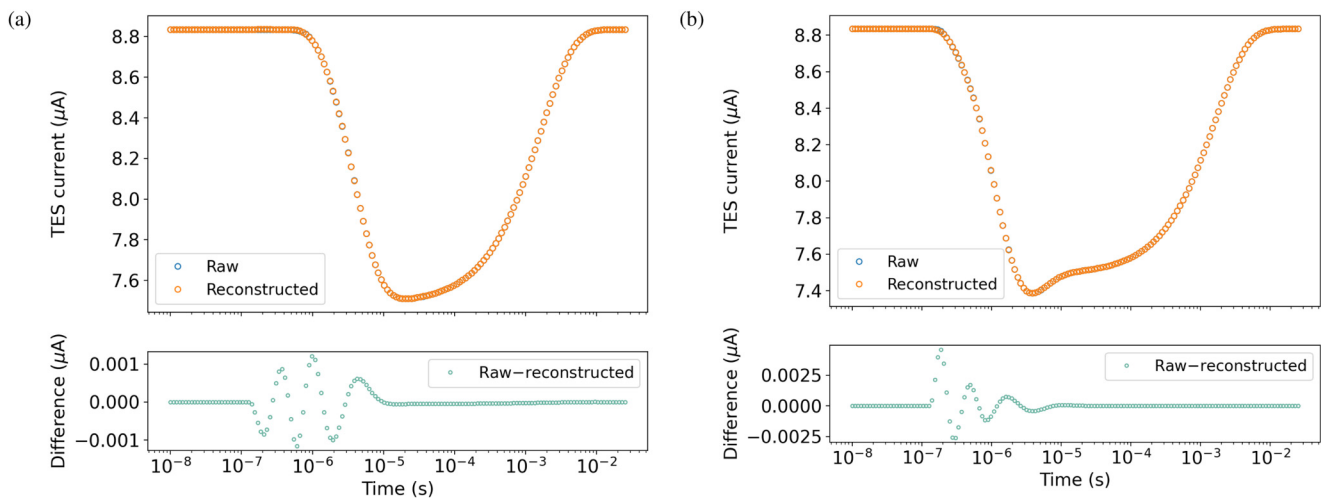

FIG. 17. PCA reconstructed pulses from two photon impact positions in the simulation: (a) far from the TES and (b) close to the TES.
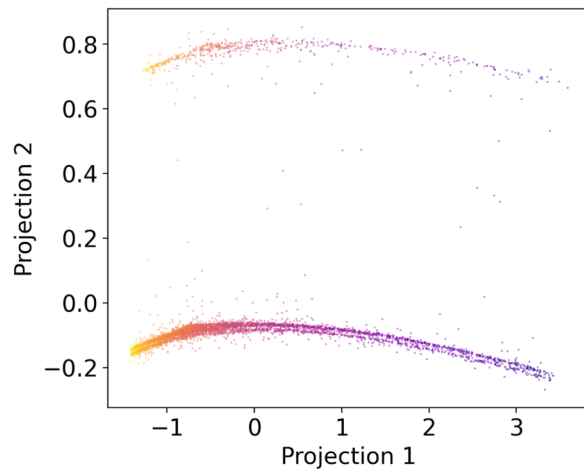
FIG. 18. Correlation between the first two principal components. The colors denote the distance to the center of the corresponding impact point as shown in Fig. 11(a).

The correlation between principal components is modeled using a polynomial fit. Subsequently, the projection distance of each data point to the fitted curve is computed, and a spectrum of the projection is shown in Fig. 19. Finally, the energy spectrum is calibrated using multiple peaks, and spectral fitting is performed using the Hölzer function[29] [see Fig. 12(b)].
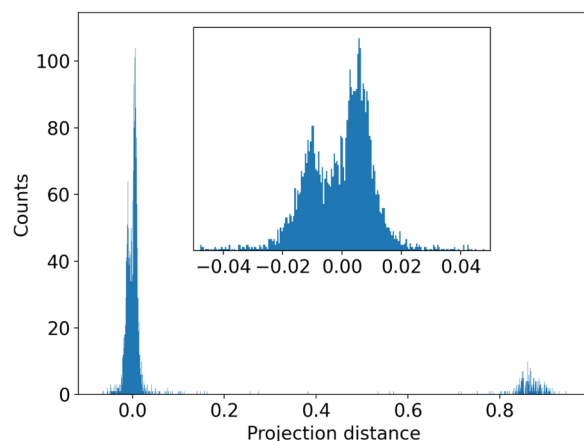

FIG. 19. Spectrum of projection distance to the correlation of the principal components. The inset shows the scaled "Kα lines" with excess broadening.

REFERENCES

[1]K. D. Irwin and G. C. Hilton, "Transition-edge sensors," in *Cryogenic particle detection* (Springer, 2005), pp. 63–150.
[2]D. McCammon, "Thermal equilibrium calorimeters—An introduction," in *Cryogenic Particle Detection*, edited by C. Enss (Springer, Berlin, 2005), pp. 1–34.
[3]A. R. Miniussi, J. S. Adams, S. R. Bandler, J. A. Chervenak, A. M. Datesman, M. E. Eckart, A. J. Ewin, F. M. Finkbeiner, R. L. Kelley, C. A. Kilbourne *et al.*, "Performance of an X-ray microcalorimeter with a 240 μm absorber and a 50 μm TES bilayer," J. Low Temp. Phys. **193**, 337–343 (2018).
[4]M. de Wit, L. Gottardi, K. Nagayoshi, H. Akamatsu, M. P. Bruijn, M. L. Ridder, E. Taralli, D. Vaccaro, J.-R. Gao, and J.-W. A. den Herder, "Performance of the SRON Ti/Au transition edge sensor x-ray calorimeters," Proc. SPIE **12181**, 121812B (2022).
[5]D. Barret, V. Albouys, J.-W. D. Herder, L. Piro, M. Cappi, J. Huovelin, R. Kelley, J. M. Mas-Hesse, S. Paltani, G. Rauw *et al.*, "The athena X-ray integral field unit: A consolidated design for the system requirement review of the preliminary definition phase," Exp. Astron. **55**, 373–426 (2023).
[6]S. J. Smith, J. S. Adams, S. R. Bandler, S. Beaumont, J. A. Chervenak, E. V. Denison, W. B. Doriese, M. Durkin, F. M. Finkbeiner, J. W. Fowler *et al.*, "Performance of a broad-band, high-resolution, transition-edge sensor spectrometer for X-ray astrophysics," IEEE Trans. Appl. Supercond. **31**, 1–6 (2021).
[7]K. Nagayoshi, M. Ridder, M. Bruijn, L. Gottardi, E. Taralli, P. Khosropanah, H. Akamatsu, S. Visser, and J.-R. Gao, "Development of a Ti/Au TES microcalorimeter array as a backup sensor for the Athena/X-IFU instrument," J. Low Temp. Phys. **199**, 943–948 (2020).
[8]W. Cui, L. B. Chen, B. Gao, F. L. Guo, H. Jin, G. L. Wang, L. Wang, J. J. Wang, W. Wang, Z. S. Wang, Z. Wang, F. Yuan, and W. Zhang, "HUBS: Hot universe baryon surveyor," J. Low Temp. Phys. **199**, 502 (2020).
[9]W. Cui, J. N. Bregman, M. P. Bruijn, L. B. Chen, Y. Chen, C. Cui, T. T. Fang, B. Gao, H. Gao, J. R. Gao, L. Gottardi, K. X. Gu, F. L. Guo, J. Guo, C. L. He, P. F. He, J. W. den Herder, Q. S. Huang, F. J. Li, J. T. Li, J. J. Li, L. Y. Li, T. P. Li, W. B. Li, J. T. Liang, Y. J. Liang, G. Y. Liang, Y. J. Liu, Z. Liu, Z. Y. Liu, F. Jaeckel, L. Ji, W. Ji, H. Jin, X. Kang, Y. X. Ma, D. McCammon, H. J. Mo, K. Nagayoshi, K. Nelms, R. Qi, J. Quan, M. L. Ridder, Z. X. Shen, A. Simionescu, E. Taralli, Q. D. Wang, G. L. Wang, J. J. Wang, K. Wang, L. Wang, S. F. Wang, S. J. Wang, T. G. Wang, W. Wang, X. Q. Wang, Y. L. Wang, Y. R. Wang, Z. Wang, Z. S. Wang, N. Y. Wen, M. de Wit, S. F. Wu, D. Xu, D. D. Xu, H. G. Xu, X. J. Xu, R. X. Xu, Y. Q. Xue, S. Z. Yi, J. Yu, L. W. Yang, F. Yuan, S. Zhang, W. Zhang, Z. Zhang, Q. Zhong, Y. Zhou, and W. X. Zhu, "HUBS: A dedicated hot circumgalactic medium explorer," Proc. SPIE **11444**, 114442S (2020).
[10]S. Wang, G. Wang, N. Chen, Y. Chen, W. Cui, J. Ding, F. Li, Y. Liang, Q. Wang, and Y. Wang, "Development of superconducting microcalorimeters for the HUBS mission," Superconductivity **4**, 100027 (2022).
[11]A. Brown, S. Bandler, R. Brekosky, J. Chervenak, E. Figueroa-Feliciano, F. Finkbeiner, N. Iyomoto, R. Kelley, C. Kilbourne, F. Porter, S. Smith, T. Saab, and J. Sadleir, "Absorber materials for transition-edge sensor X-ray microcalorimeters," J. Low Temp. Phys. **151**, 413–417 (2008).
[12]J. Vaillancourt, C. Allen, R. Brekosky, A. Dosaj, M. Galeazzi, R. Kelley, D. Liu, D. McCammon, F. Porter, L. Rocks, W. Sanders, and C. Stahle, "Large area bismuth absorbers for X-ray microcalorimeters," Nucl. Instrum. Methods Phys. Res., Sect. A **520**, 212–215 (2004).
[13]N. Iyomoto, S. Bandler, R. Brekosky, J. Chervenak, E. Figueroa-Feliciano, F. Finkbeiner, R. Kelley, C. Kilbourne, M. Lindeman, K. Murphy, F. Porter, T. Saab, J. Sadleir, and D. Talley, "Position-sensitive transition-edge sensors," Nucl. Instrum. Methods Phys. Res., Sect. A **559**, 491–493 (2006).
[14]T. Saab, E. Figueroa-Feliciano, N. Iyomoto, S. R. Bandler, J. A. Chervenak, R. L. Kelley, C. A. Kilbourne, F. S. Porter, and J. E. Sadleir, "Determining the thermal diffusivity in microcalorimeter absorbers and its effect on detector response," J. Appl. Phys. **102**, 104502 (2007).
[15]T. Oshima and H. Yoshitake, "Optimization method for tes microcalorimeters with absorbers," IEEE Trans. Appl. Supercond. **19**, 465–468 (2009).

[16]K. M. Morgan, "Transition-edge sensor microcalorimeters for a diffuse soft X-ray sounding rocket mission," Ph.D. thesis (University of Wisconsin, Madison, 2015).

[17]R. Ota, K. Tanaka, T. Hayashi, R. Miyagawa, Y. Yagi, N. Y. Yamasaki, and K. Mitsuda, "Electro-thermal simulation and evaluation of transition edge sensor X-ray microcalorimeter with mushroom-type absorber," J. Low Temp. Phys. **217**, 366–373 (2024).

[18]COMSOL Multiphysics v. 6.0, COMSOL AB, Stockholm, Sweden (2021).

[19]S. Moseley, R. Kelley, R. Schoelkopf, A. Szymkowiak, D. McCammon, and J. Zhang, "Advances toward high spectral resolution quantum X-ray calorimetry," IEEE Trans. Nucl. Sci. **35**, 59–64 (1988).

[20]S. Busch, J. Adams, S. Bandler, J. Chervenak, M. Eckart, F. Finkbeiner, D. Fixsen, R. Kelley, C. Kilbourne, S.-J. Lee, S. Moseley, J. Porst, F. Porter, J. Sadleir, and S. Smith, "Progress towards improved analysis of TES X-ray data using principal component analysis," J. Low Temp. Phys. **184**, 382–388 (2016).

[21]D. Yan, T. Cecil, L. Gades, C. Jacobsen, T. Madden, and A. Miceli, "Processing of X-ray microcalorimeter data with pulse shape variation using principal component analysis," J. Low Temp. Phys. **184**, 397–404 (2016).

[22]C. P. de Vries, R. M. Schouten, J. van der Kuur, L. Gottardi, and H. Akamatsu, "Microcalorimeter pulse analysis by means of principle component decomposition," Proc. SPIE **9905**, 99055V (2016).

[23]J. Fowler, B. Alpert, Y.-I. Joe, G. O'Neil, D. Swetz, and J. Ullom, "A robust principal component analysis for outlier identification in Messy microcalorimeter data," J. Low Temp. Phys. **199**, 745–753 (2020).

[24]A. Kozorezov, A. A. Golubov, D. D. E. Martin, P. A. J. de Korte, M. A. Lindeman, R. A. Hijmering, J. van der Kuur, H. F. C. Hoevers, L. Gottardi, M. Y. Kupriyanov, and J. K. Wigmore, "Modelling the resistive state in a transition edge sensor," Appl. Phys. Lett. **99**, 063503 (2011).

[25]H. F. C. Hoevers, M. L. Ridder, A. Germeau, M. P. Bruijn, P. A. J. de Korte, and R. J. Wiegerink, "Radiative ballistic phonon transport in silicon-nitride membranes at low temperatures," Appl. Phys. Lett. **86**, 251903 (2005).

[26]M. de Wit, L. Gottardi, E. Taralli, K. Nagayoshi, M. Ridder, H. Akamatsu, M. Bruijn, R. Hoogeveen, J. van der Kuur, K. Ravensberg, D. Vaccaro, J.-R. Gao, and J.-W. den Herder, "Impact of the absorber-coupling design for transition-edge-sensor X-ray calorimeters," Phys. Rev. Appl. **16**, 044059 (2021).

[27]C. V. Ambarish, F. T. Jaeckel, E. John, W. Liu, D. McCammon, A. Roy, H. R. Stueber, Z. Wang, and T. Yan, "Large, thin, and corrugated gold absorbers for transition edge sensor microcalorimeters," IEEE Trans. Appl. Supercond. **33**, 1–5 (2023).

[28]E. Figueroa-Feliciano, "Complex microcalorimeter models and their application to position-sensitive detectors," J. Appl. Phys. **99**, 114513 (2006).

[29]G. Hölzer, M. Fritsch, M. Deutsch, J. Härtwig, and E. Förster, "$K\alpha_{1,2}$ and $K\beta_{1,3}$ X-ray emission lines of the $3d$ transition metals," Phys. Rev. A **56**, 4554 (1997).

28 July 2025 12:20:16